

Impact of reflection Comptonization on X-ray reflection spectroscopy: the case of EXO 1846–031

Songcheng Li,¹ Honghui Liu,¹ Cosimo Bambi,^{1,2,*} James F. Steiner,³ and Zuobin Zhang¹

¹*Center for Astronomy and Astrophysics, Center for Field Theory and Particle Physics, and Department of Physics, Fudan University, Shanghai 200438, China*

²*School of Natural Sciences and Humanities, New Uzbekistan University, Tashkent 100007, Uzbekistan*

³*Center for Astrophysics, Harvard & Smithsonian, Cambridge, MA 02138, United States*

Within the disk-corona model, it is natural to expect that a fraction of reflection photons from the disk are Compton scattered by the hot corona (reflection Comptonization), even if this effect is usually ignored in X-ray reflection spectroscopy studies. We study the effect by using *NICER* and *NuSTAR* data of the Galactic black hole EXO 1846–031 in the hard-intermediate state with the model `simplcutx`. Our analysis suggests that a scattered fraction of order 10% is required to fit the data, but the inclusion of reflection Comptonization does not change appreciably the measurements of key-parameters like the black hole spin and the inclination angle of the disk.

I. INTRODUCTION

In the disk-corona model, a black hole accretes from a geometrically thin and optically thick accretion disk, as shown in Fig. 1 [1–4]. The disk can be described by the Novikov-Thorne model [5] and has a multicolor blackbody spectrum. A portion of the thermal photons are subsequently scattered by hot electrons residing in the corona, yielding a power-law component in the spectrum. The power-law component illuminates the disk, thereby producing a reflection component marked by fluorescent emission lines in the soft X-ray band and a Compton hump with a peak at 20–30 keV [6, 7]. With high quality data and the correct astrophysical model, X-ray reflection spectroscopy can be a powerful tool to study the morphology of the accreting system and the spacetime around the black hole [1].

The corona plays a vital role in the process of spectrum generation within this paradigm. In the Comptonization of photons emitted from the accretion disk, we often consider Comptonization of thermal photons from the disk, ignoring the reflection photons. Reflection photons should also undergo Compton scattering off electrons in the corona above the accretion disk [8, 9], as shown in Fig. 1 by the magenta arrow. Such a reflection Comptonization seems to be unavoidable, but it is normally overlooked in the spectral analysis of accreting black holes. Wilkins and Gallo [10] showed that an extended corona in active galactic nuclei (AGN) should scatter the reflection photons and a similar conclusion can be expected in the case of stellar-mass black holes in X-ray binary systems. The fraction of reflection photons that are Compton scattered by the corona should depend on the extension of the corona and its optical depth. If the corona covers a sufficiently large fraction of the inner part of the accretion disk and its optical depth is not low, the reflection Comptonization is expected to have

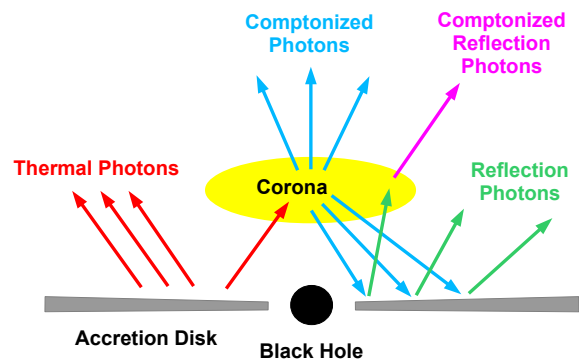


FIG. 1. Disk-corona system with reflection Comptonization.

an impact on the spectral analysis and on the estimates of the properties of the accreting system.

In this paper, we present a study of the impact of the reflection Comptonization on the analysis of a reflection dominated spectrum of a Galactic black hole, EXO 1846–031. We use `simplcutx` [9] to describe any Compton scattering in the corona. We compare the measurements of the properties of the spectrum with and without including the effect of reflection Comptonization.

EXO 1846–031 is a black hole X-ray binary discovered by *EXOSAT* on April 3, 1985 [11]. After a quiescent period of over two decades, it experienced a new outburst in 2019, which was first detected by *MAXI/GSC* on July 23, 2019 [12]. This outburst was also observed by other missions during the following few weeks, such as *Swift* [13], *NICER* [14], and *NuSTAR* [15]. During the hard to soft state transition [16], the source showed a spectrum with strong reflection features [15] and quasi-periodic oscillations (QPOs) [17]. Draghis *et al.* [18] found that the black hole in EXO 1846–031 has a spin parameter very close to 1 and the viewing angle of its accretion disk is high, close to 70 deg. Thanks to the very strong reflection features in the *NuSTAR* spectrum, this source has been widely used to test new reflection models (see, e.g.,

* Corresponding author: bambi@fudan.edu.cn

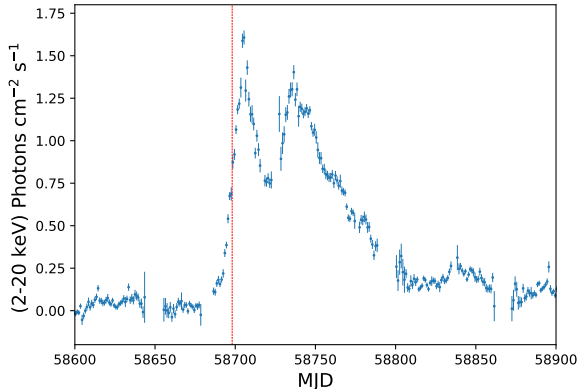


FIG. 2. Light curve of EXO 1846–031 from Monitor of All-sky X-ray Image (MAXI)^b. The red-dashed line marks the observation date of the data we used.

Refs. [19, 20]) as well as different spacetime metrics from modified gravity theories (see, e.g., Refs. [21–24]). Abdikamalov *et al.* [19] showed that a radial disk ionization profile can improve the fit of the spectrum around 7 keV. QPOs were studied in Liu *et al.* [25] and the possible existence of a disk wind was studied in Wang *et al.* [26].

Past studies have shown that EXO 1846–031 exhibits strong reflection features. In the present manuscript, we still analyze the *NuSTAR* spectrum of the 2019 outburst, but we also incorporate soft X-ray data from *NICER* and perform joint fitting analysis to explore whether this will lead to any differences in the final results.

The content of the manuscript is as follows. In Section II, we present the observation information and data reduction process. In Section III, we describe the two model configurations to study the impact of reflection Comptonization and present the spectral analysis results of the observation of EXO 1846–031. We discuss our results in Section IV and present our conclusions in Section V.

II. OBSERVATIONS AND DATA REDUCTION

EXO 1846–031 was observed by *NuSTAR* and *NICER* on August 3, 2019. The source was in a transitional phase from hard state to intermediate state [27]. The X-ray flux was about 46% of the soft state peak (see Fig. 2). The details of the observations analyzed in our work are shown in Table I.

For the *NuSTAR* observation, we reduced the data with NuSTARDAS and the CALDB 20220301 [28]. We selected a circular region with a radius of 180'' on both focal plane module A (FPMA) and focal plane module B

(FPMB) detectors to extract the source spectra. In order to prevent influence from the source photons, a background region of comparable size was selected far from the source region. Afterwards, we used *nuproducts* to generate the source and background spectra. We grouped the spectra with the optimal binning algorithm in [29] by using the *ftgrouppha* task.

For the *NICER* observation, the *NICERDAS* software suite was used to process the data. Extractions used standard screenings for the Sun angle, bright-Earth limb, and boresight. Any South Atlantic Anomaly (SAA) passages were excised. Data from detectors 14, 34, and 54, were screened out, owing to intermittent calibration issues manifest from those detectors. All other of *NICER*'s 49 additional working detectors were on, and from this set of events the detector ensemble distribution of X-ray events, undershoots, and overshoots were separately compared. There were no significant outliers, and so the remaining 49 active detectors were all used for spectral extraction. Undershoot levels were low for the observation in question, which ensures the robustness of the gain solution. The spectrum was adaptively binned to oversample the instrumental resolution by a factor of 2-3, and include at least 5 counts per bin. The 3C50 background model [30] was used to produce background spectra.

III. DATA ANALYSIS

We use XSPEC v12.12.1 [31] to analyze the spectra. We use two different datasets for the spectral fitting process: the spectra from *NuSTAR* only (our “*NuSTAR* data”), and the spectra from both *NuSTAR* and *NICER* (our “*NuSTAR+NICER* data”) for a joint fitting. The reason is to demonstrate the influence of soft X-ray data on the fitting. The fits are made across the 3.0-79.0 keV energy band of *NuSTAR* and the 1.0-10.0 keV energy band for *NICER*. In the joint fitting of *NuSTAR* and *NICER* data, *NuSTAR* data below 4.5 keV are ignored in order to avoid the mismatch between *NICER* and *NuSTAR* at the low energy band, as demonstrated by other studies [32, 33].

Firstly, we fit the data with an absorbed disk blackbody and power-law to see the reflection features in the spectrum. In XSPEC language, the model reads

$$\text{tbabs} * (\text{diskbb} + \text{nthcomp}), \quad (1)$$

where *tbabs* describes the galactic absorption with the abundance table from [34], *diskbb* [35, 36] describes the thermal component, and *nthcomp* [37, 38] describes the power-law component. We link T_{in} in *diskbb* to T_{bb} in *nthcomp*. We clearly see reflection features with a broad iron line around 7 keV and a Compton hump peaking around 20-30 keV (Fig. 3).

¹ Light curve data:

http://maxi.riken.jp/star_data/J1849-030/J1849-030.html

TABLE I. List of the observations analyzed in this paper.

Source	Mission	Observation ID	Observation Time	Exposure (ks)	Count rate (s ⁻¹)
EXO 1846–031	<i>NuSTAR</i>	90501334002	2019-08-03 02:01:09	22.2	148.7
	<i>NICER</i>	2200760104	2019-08-03 02:08:58	0.911	376.1

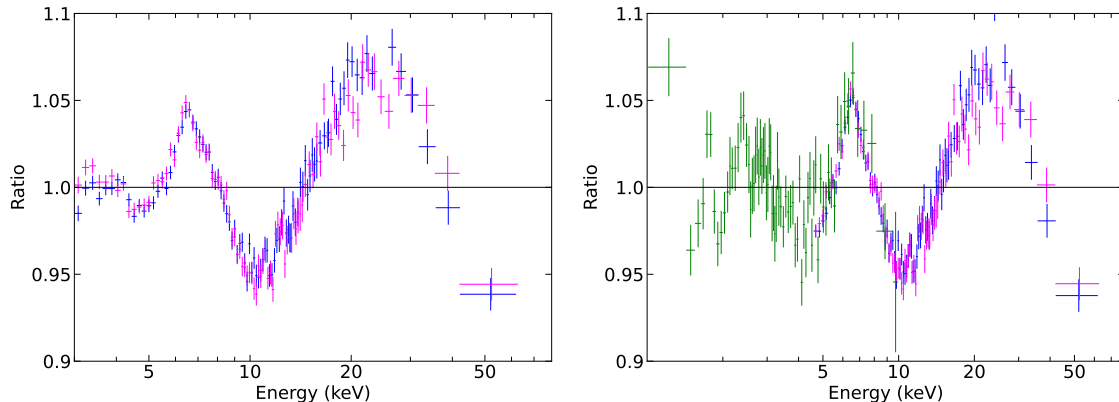


FIG. 3. Data to best-fit model ratio plots for an absorbed disk blackbody and power-law model. The left panel is for *NuSTAR* data and the right panel is for *NuSTAR*+*NICER* data. The blue and purple crosses are for the FPMA/*NuSTAR* and FPMB/*NuSTAR* data and the green crosses are for the *NICER* data.

A. Model 1: conventional modeling

Previous study on the same observation shows that a reflection model that assumes a radial ionization gradient can fit the data better [19]. Therefore, we implement the `relxillion_nk` model which describes the ionization profile with a power-law:

$$\xi(r) = \xi_0 \left(\frac{R_{\text{in}}}{r} \right)^{\alpha_\xi}, \quad (2)$$

where ξ_0 is the value of the ionization parameter at the inner edge of the disk, R_{in} is the radial coordinate of the inner edge of the disk, and α_ξ is the index of the power-law ionization profile. The total model is `tbabs*(diskbb+nthcomp+relxillionCp_nk)` (Model 1), where `relxillionCp_nk` is a flavor of `relxillion_nk` that uses the `nthcomp` Comptonization continuum for the incident spectrum.

B. Model 2: self-consistent modeling with `simplcutx`

Adopting a more self-consistent model structure, the power-law component is generated from Comptonization of the thermal component in the corona, and the reflection component originating from the disk surface will also be Comptonized [9]. In XSPEC language, the model expression is `tbabs*simplcutx*(diskbb+relxillionCp_nk)`

(Model 2). We set the reflection fraction R_{F} in `simplcutx` as 1 to avoid parameter degeneracy. In `simplcutx`, R_{F} is defined as the number of scattered photons that return to illuminate the disk divided by the number of photons that reach infinity.

C. Analysis for the emissivity profile

The emissivity profile depends on the geometry of the corona, which is unknown. Therefore, we model the emissivity profile using an empirical broken power-law ($\epsilon \propto 1/r^{q_{\text{in}}}$ for $r < R_{\text{break}}$, $\epsilon \propto 1/r^{q_{\text{out}}}$ for $r > R_{\text{break}}$). In previous studies on EXO 1846–031 [18, 19], the authors found that the *NuSTAR* data can be fit well with a broken power-law emissivity profile with a high inner emissivity index ($q_{\text{in}} \approx 10$) and an almost flat emissivity profile ($q_{\text{out}} \approx 0$) at larger radii. We note that the luminosity of an infinite disk is finite only if $q_{\text{out}} > 2$. Moreover, the theoretical reflection spectrum will obviously change with the variation of the disk’s outer radius R_{out} if q_{out} is close to zero in reflection models like `relxill_nk`. This means that in our case with $q_{\text{out}} \approx 0$ the reflection spectrum does depend on the exact value of the outer radial coordinate of the disk (see Fig. 4 for an example).

Since the maximum value of the outer radius of the disk in our reflection model is 900 gravitational radii (R_{g}) and if we leave it free it seems like the fit requires a larger value than this, we consider three different scenarios: q_{out}

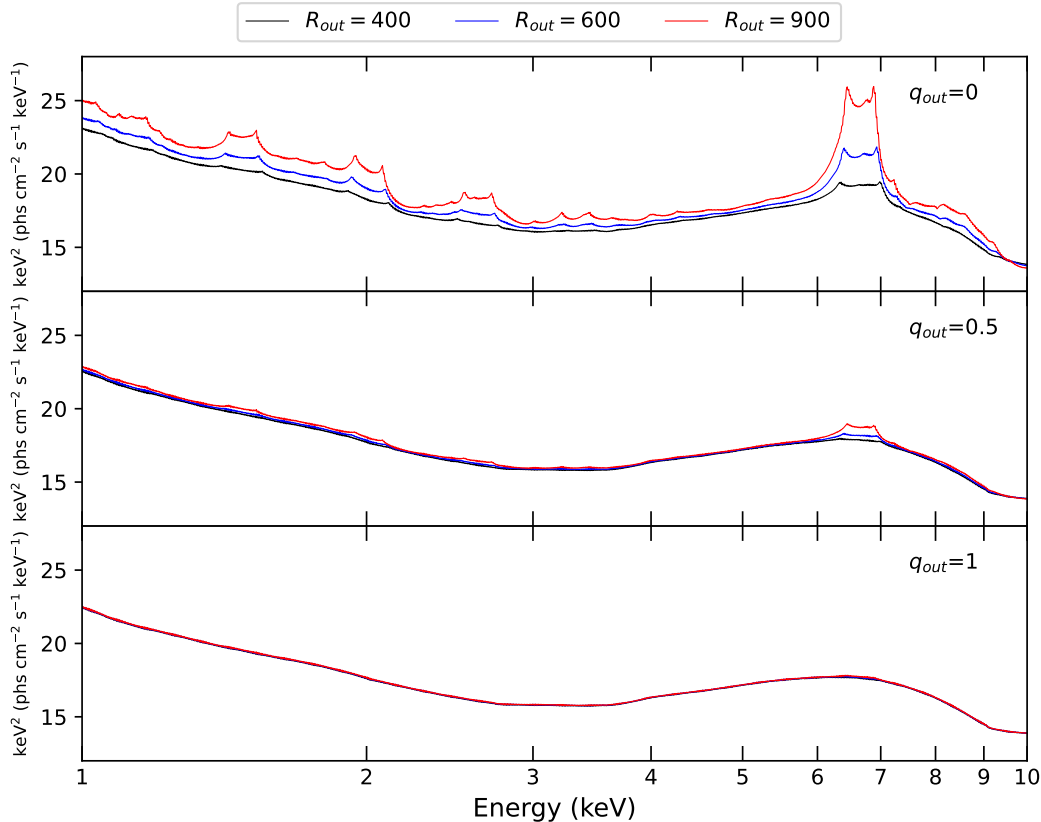


FIG. 4. Relativistic reflection spectra with different values of q_{out} and R_{out} . In all of these plots, the other parameters are set to the same specific values: $q_{in} = 10$, $R_{br} = 6 R_g$, $R_{in} = R_{ISCO}$, $a_* = 0.998$, $i = 75^\circ$, $\Gamma = 2$, $E_{cut} = 100$ keV, $\log \xi = 3.1$, $A_{Fe} = 1$.

is free (case A), $q_{out} = 3$ (case B), q_{out} is free and we add a distant reflector with `xillverCp`, in which the ionization parameter is low ($\log \xi = 0$; case C). We set R_{out} to its maximum value in the model in order to be sensitive even to the radiation emitted at relatively large radii.

All models we tested are summarized in Table II.

D. Other setting and final results

For the *NuSTAR* data, we only set a cross-calibration constant between FPMA and FPMB. For the *NuSTAR*+*NICER* data, we add an `edge` component to fit an absorption edge around 1.84 keV. We also apply the `xscat` model [39] for all data as the field of view of *NICER* is comparable to the typical size of a dust scattering halo. We choose the MRN dust model for the scattering. For the extraction regions, the radius is $50''$ for the *NuSTAR* data and $180''$ for the *NICER* data, in accordance with the configuration in [40]. Furthermore, we apply a cross-calibration model called `crabber` [41] which is designed to standardize the calibration parameters between different detectors for the Crab Nebula (power-law normalization and index) via a multiplicative power-law

correction. All parameters in the *NuSTAR* and *NICER* spectra are linked except the cross-calibration parameters.

For both Model 1 and Model 2, we link Γ and kT_e between the power-law component (`simplcutx` or `nthcomp`) and the reflection component (`relxillionCp_nk` and `xillverCp`). The reflection fraction R_f in `relxillionCp_nk` is set to -1 , so the model returns only the reflection component. We also link the neutral column in `xscat` to the value from `tbabs`.

We apply the AICc [42], which is the Akaike information criterion (AIC) [43] corrected for small sample sizes and provides a mean for selecting the best model among several model candidates. The model candidate with the lowest AICc is the best model. The formulas used to calculate AIC and AICc are

$$\text{AIC} = -2\ln\mathcal{L} + 2N_p \quad (3)$$

and

$$\text{AICc} = \text{AIC} + 2N_p(N_p + 1)/(N_b - N_p - 1), \quad (4)$$

where N_p is the number of free parameters, N_b is the number of bins and \mathcal{L} is the likelihood of the best-fit

TABLE II. Models used to analyze the *NuSTAR* data of EXO 1846–031. As for the *NuSTAR+NICER* data, we just replace `constant` with `crabber*edge*xscat`.

model	q_{out}	XSPEC model for <i>NuSTAR</i> data
1A	free	<code>constant*tbabs*(diskbb + nthcomp + relxillionCp_nk)</code>
1B	3*	<code>constant*tbabs*(diskbb + nthcomp + relxillionCp_nk)</code>
1C	free	<code>constant*tbabs*(diskbb + nthcomp + relxillionCp_nk + xillverCp)</code>
2A	free	<code>constant*tbabs*simplcutx*(diskbb + relxillionCp_nk)</code>
2B	3*	<code>constant*tbabs*simplcutx*(diskbb + relxillionCp_nk)</code>
2C	free	<code>constant*tbabs*(simplcutx*(diskbb + relxillionCp_nk)+xillverCp)</code>

model. The values of likelihood can be written in terms of χ^2 which is obtained from the model’s best fit: $\chi^2 = -2 \ln \mathcal{L}$.

For the *NuSTAR* data, the best-fit for all models are presented in Table III and the best-fit model plots and residual plots are presented in Fig. 5.

As for the *NuSTAR+NICER* data, the best-fit for all models are presented in Table IV and the best-fit model plots and residual plots are presented in Fig. 6. In addition, for all the plots of best-fit models with `simplcutx`, we also plot the scattered and transmitted spectra separately.

IV. DISCUSSION

A. Impact of reflection Comptonization

In our study, we use *NICER* and *NuSTAR* data of EXO 1846–031 to investigate the impact of Comptonization of the reflection component on the measurements of the spectral parameters. In Model 2, the Comptonized reflection spectrum is produced by `simplcutx*relxillionCp_nk`, while there is no Comptonized reflection spectrum in Model 1.

We do not see significant differences in the parameter estimation between Model 1 and Model 2 (Table III and Table IV). The key-parameters, such as a_* and i , are quite similar at 3σ confidence level (see Fig. 7), indicating that the parameter measurements are not affected. In addition, the reduced χ^2 and AICc are also very close to each other. Possibly, stronger differences in those key parameters would manifest in the case of larger f_{SC} (viz: $f_{\text{SC}} > 0.2$). Other studies also suggest that the inclusion of reflection Comptonization does not significantly influence reflection spectrum fitting; see, e.g., Refs. [44–46].

The scattered fraction f_{SC} in `simplcutx` depends on the coronal geometry and optical depth. Liu *et al.* [45] found that the scattering fraction decreases during the hard-to-soft transition of GX 339–4 in the outburst in 2021 observed by *Insight-HXMT*. Wang *et al.* [47] studied the reverberation lag of EXO 1846–031 to infer the disk-corona geometry and concluded that the corona may

be the base of the jet and that the vertical extension of the jet changes during the hard-to-soft transition. These studies support the idea of an evolving corona across state transition in X-ray binaries, one measure of which is the scattering fraction. In this case, although the model formalism with `simplcutx` does not improve the fit statistically, in such a case looking for changes of f_{SC} with state may provide its own useful consistency check.

B. Impact of soft X-ray data

From the comparison of the results from the analyses of the *NuSTAR* and *NuSTAR+NICER* data, we see the impact of the soft X-ray band in the analysis of the data. The disk component peaks around 2.0–3.0 keV (see Fig. 6), but *NuSTAR* lacks coverage below 3.0 keV. Consequently, the fit of the disk component with *NuSTAR* data may not be as accurate as the fit with *NuSTAR+NICER* data. In terms of parameters estimation, while some parameters differ slightly (e.g. N_{H} , T_{in}), key parameters such as spin and inclination angle still do not change significantly. It is tentatively suggested that the inclusion of soft X-ray data does not significantly impact the parameter estimations of the best-fit model. However, by including *NICER* soft X-ray data, we identify an additional χ^2 minimum, not as deep, which exhibits a more reasonable flux of the disk component despite having a slightly higher AICc; see the columns of Models 1A-2 and 2A-2 in Table IV.

The mass and distance of EXO 1846-031 have not been dynamically measured yet. Studies of spectral analysis suggest mass measurements ranging from 3.24 to 7.1–12.43 M_{\odot} [33, 48], and distance measurements ranging from 2.4 to 7 kpc [49, 50]. Considering a distance of 7 kpc and a mass in the range 5 to 12 M_{\odot} , the Eddington ratio L/L_{Edd} is 21.6%–51.7% for Model 1A-1, 18%–43% for Model 2A-1, 7.7%–13% for Model 1A-2, and 7.8%–13% for Model 2A-2. Furthermore, the unabsorbed disk component is much fainter in Models 1A-2 and 2A-2 (refer to the “disk/total” row in Table IV). This indicates that for certain values of mass and distance, the luminosity of Models 1A-1 and 2A-1 is too high, while the results of

FIG. 5. Model and residual plots for EXO 1846–031 with *NuSTAR* data. In the left panel, the red lines represent the thermal components, the blue lines represent the power-law components, and orange lines represent the reflection components. In the right panel, the blue lines represent the Comptonized thermal spectra, and the orange lines represent the Comptonized reflection spectra. For the lines with same color, solid lines represent the complete spectra, dotted lines represent the components scattered by the corona, and dashed lines represent the components transmitted by the corona.

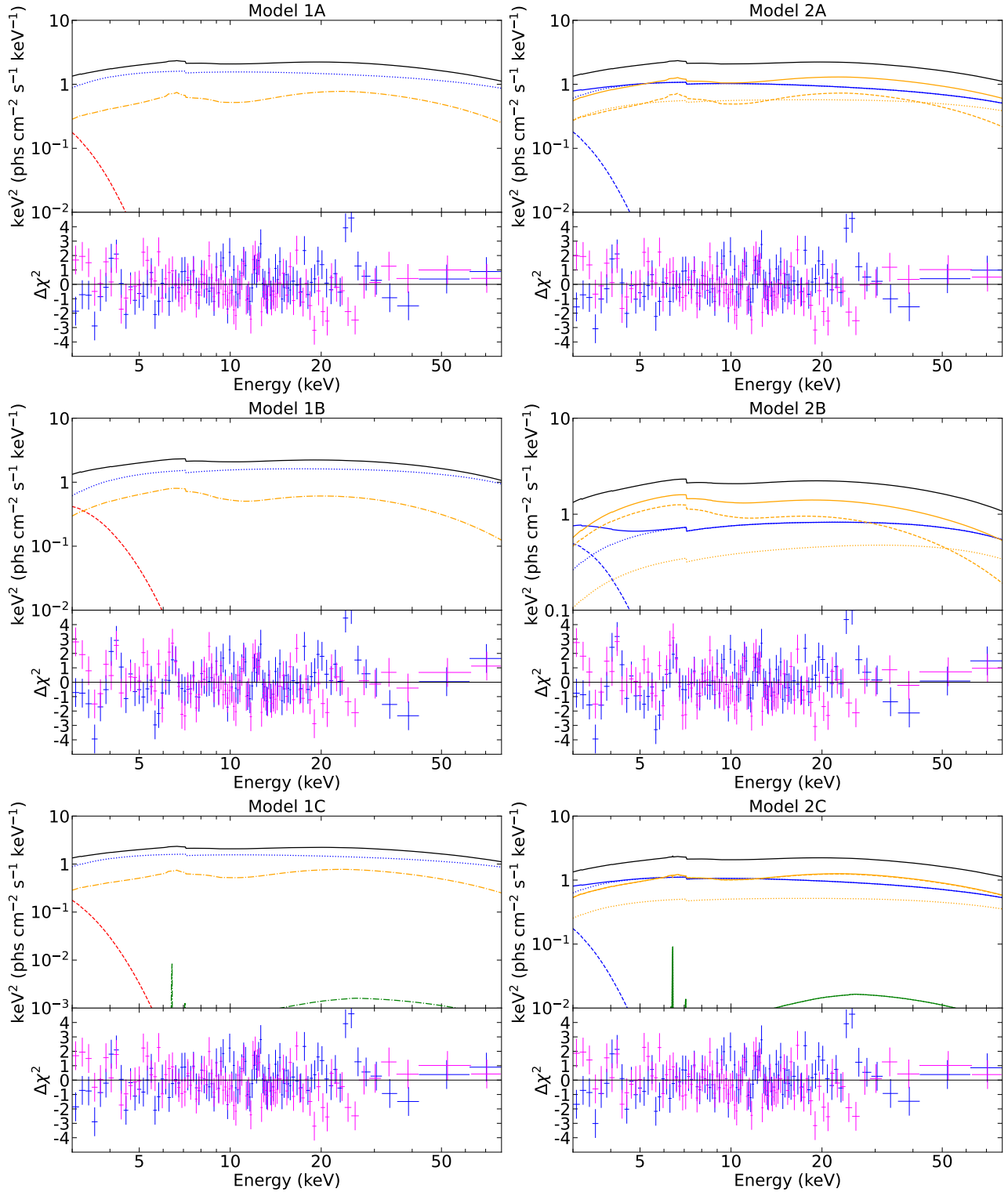


TABLE III. Best-fit values of all models with *NuSTAR* data. *P* means that we reach the lower or upper limit of the model.

Model	Model 1A	Model 1B	Model 1C	Model 2A	Model 2B	Model 2C
tbabs						
N_{H} [10^{22} cm $^{-2}$]	$7.7^{+0.5}_{-0.5}$	$9.7^{+0.4}_{-0.6}$	$7.66^{+0.5}_{-0.21}$	$7.7^{+0.5}_{-0.6}$	$10.5^{+0.6}_{-0.5}$	$7.7^{+0.6}_{-0.4}$
diskbb						
T_{in}	$0.33^{+0.04}_{-0.04}$	$0.452^{+0.011}_{-0.011}$	$0.33^{+0.04}_{-0.06}$	$0.349^{+0.019}_{-0.014}$	$0.459^{+0.011}_{-0.004}$	$0.337^{+0.012}_{-0.015}$
Norm	$1.1^{+2.4}_{-0.6} \times 10^5$	$1.88^{+0.23}_{-0.4} \times 10^4$	$1.1^{+2.3}_{-0.6} \times 10^5$	$8.6^{+6}_{-1.8} \times 10^4$	$2.48^{+0.23}_{-0.4} \times 10^4$	$1.13^{+0.25}_{-0.11} \times 10^5$
simplcutx						
Γ				$2.139^{+0.012}_{-0.014}$	$1.9345^{+0.03}_{-0.0026}$	$2.14^{+0.03}_{-0.02}$
kT_{e} [keV]				$58.7^{+9}_{-16.3}$	$31.6^{+1.8}_{-1.6}$	$66^{+30.0}_{-18.8}$
f_{sc}				$0.215^{+0.013}_{-0.026}$	$0.120^{+0.024}_{-0.04}$	$0.196^{+0.015}_{-0.03}$
nthcomp						
Γ	$2.102^{+0.028}_{-0.015}$	$1.986^{+0.007}_{-0.011}$	$2.102^{+0.024}_{-0.04}$			
kT_{e} [keV]	$61^{+26.9}_{-17.8}$	$31.1^{+4}_{-2.1}$	$61^{+17.6}_{-20.7}$			
Norm	$1.70^{+0.16}_{-0.13}$	$1.12^{+0.03}_{-0.13}$	$1.70^{+0.16}_{-0.14}$			
relxillionCp.nk						
q_{in}	$9.8^{+P}_{-2.1}$	$10.0^{+P}_{-0.3}$	$9.8^{+P}_{-2.1}$	$9.5^{+0.4}_{-1.4}$	$10.0^{+P}_{-1.4}$	$9.5^{+0.5}_{-1.7}$
q_{out}	$0.17^{+0.9}_{-P}$	3*	$0.17^{+1.1}_{-P}$	$0.0011^{+1.1}_{-P}$	3*	$0.8^{+0.3}_{-0.4}$
R_{br} [R_{g}]	$6.6^{+2.9}_{-1.4}$	$3.00^{+0.29}_{-0.12}$	$6.6^{+1.0}_{-1.5}$	$7.5^{+1.2}_{-0.9}$	$3.18^{+0.4}_{-0.17}$	$5.1^{+1.7}_{-1.5}$
a_*	$0.9912^{+0.0019}_{-0.0028}$	$0.973^{+0.005}_{-0.016}$	$0.9912^{+0.002}_{-0.0026}$	$0.9914^{+0.003}_{-0.0022}$	$0.953^{+0.023}_{-0.024}$	$0.9918^{+0.0022}_{-0.0027}$
i [deg]	$76.5^{+1.2}_{-1.5}$	$67.7^{+1.4}_{-2.7}$	$76.5^{+1.3}_{-0.5}$	$76.4^{+0.6}_{-0.6}$	$62.7^{+7}_{-2.4}$	$76.8^{+1.4}_{-0.6}$
A_{Fe}	$0.88^{+0.18}_{-0.15}$	$2.20^{+0.28}_{-0.5}$	$0.88^{+0.21}_{-0.08}$	$0.91^{+0.3}_{-0.17}$	$10.0^{+P}_{-1.3}$	$0.88^{+0.5}_{-0.06}$
α_{ξ}	$0.18^{+0.05}_{-0.04}$	$0.001^{+0.08}_{-P}$	$0.178^{+0.019}_{-0.05}$	$0.176^{+0.026}_{-0.028}$	$0.14^{+0.16}_{-P}$	$0.18^{+0.04}_{-0.05}$
$\log \xi$ [erg cm s $^{-1}$]	$3.13^{+0.18}_{-0.11}$	$3.60^{+0.1}_{-0.08}$	$3.13^{+0.12}_{-0.11}$	$3.10^{+0.12}_{-0.04}$	$4.52^{+0.04}_{-0.16}$	$3.10^{+0.19}_{-0.07}$
Norm	$0.0061^{+0.0011}_{-0.0009}$	$0.0038^{+0.0003}_{-0.0003}$	$0.0061^{+0.001}_{-0.0006}$	$0.0083^{+0.0009}_{-0.0012}$	$0.00526^{+0.0008}_{-0.00024}$	$0.0083^{+0.0012}_{-0.0018}$
xillverCp						
Norm			$0.0001^{+0.004}_{-P}$			$0.0012^{+0.002}_{-P}$
C_{FPMB}	$1.0152^{+0.0014}_{-0.0014}$	$1.0152^{+0.0014}_{-0.0014}$	$1.0152^{+0.0014}_{-0.0014}$	$1.0152^{+0.0014}_{-0.0014}$	$1.0152^{+0.0014}_{-0.0014}$	$1.0152^{+0.0013}_{-0.0014}$
χ^2 /dof	633.03/513 =1.23398	695.0/514 =1.35214	633.0/512 =1.23633	632.85/513 =1.23363	701.7/514 =1.36518	632.7/512 =1.23574
AICc	666.09	725.94	668.2	665.91	732.64	667.9

TABLE IV. Best-fit values and unabsorbed flux of all models with *NuSTAR*+*NICER* data. P means that we reach the lower or upper limit of the model. In the estimate of the Eddington ratio (last row), D is the distance in the unit of kpc and M is the mass in the unit of M_{\odot} . The estimate of the total flux is obtained by integrating the total spectrum of the best-fit model from 0.01 to 1000 keV.

Model	Model 1A-1	Model 2A-1	Model 1A-2	Model 2A-2
edge				
τ_{\max}	$0.095^{+0.026}_{-0.022}$	$0.098^{+0.015}_{-0.018}$	$0.122^{+0.016}_{-0.015}$	$0.115^{+0.024}_{-0.014}$
tbabs				
N_{H} [10^{22} cm $^{-2}$]	$6.33^{+0.09}_{-0.1}$	$6.48^{+0.11}_{-0.11}$	$5.60^{+0.29}_{-0.05}$	$5.82^{+0.07}_{-0.19}$
xscat				
x	$1.00^{+P}_{-0.05}$	$1.00^{+P}_{-0.05}$	$0.90^{+0.08}_{-0.12}$	$0.99^{+P}_{-0.13}$
diskbb				
T_{in}	$0.192^{+0.008}_{-0.01}$	$0.202^{+0.006}_{-0.01}$	$0.42^{+0.03}_{-0.06}$	$0.40^{+0.04}_{-0.09}$
Norm	$6.2^{+2.8}_{-2.7} \times 10^5$	$7.59^{+4}_{-0.04} \times 10^5$	1098^{+2152}_{-668}	1875^{+2723}_{-1156}
simplcutx				
Γ		$2.098^{+0.017}_{-0.007}$		$1.907^{+0.023}_{-0.007}$
kT_e [keV]		$44.3^{+1.4}_{-5}$		$36.1^{+6}_{-1.8}$
f_{sc}		$0.229^{+0.08}_{-0.028}$		$0.150^{+0.021}_{-0.04}$
nthcomp				
Γ	$2.052^{+0.026}_{-0.004}$		$1.875^{+0.007}_{-0.007}$	
kT_e [keV]	$38.0^{+1.6}_{-2.5}$		$41.4^{+1.2}_{-1.8}$	
Norm	$1.935^{+0.018}_{-0.012}$		$0.376^{+0.14}_{-0.015}$	
relxillionCp_nk				
q_{in}	$10.0^{+P}_{-1.4}$	$10.00^{+P}_{-0.22}$	$9.8^{+P}_{-0.9}$	$9.9^{+P}_{-0.7}$
q_{out}	$0.46^{+0.6}_{-0.12}$	$0.52^{+0.15}_{-0.09}$	$1.44^{+0.08}_{-0.26}$	$1.259^{+0.028}_{-0.5}$
R_{br} [R_{g}]	$5.59^{+0.2}_{-0.26}$	$5.5^{+0.8}_{-0.3}$	$4.45^{+0.8}_{-0.29}$	$5.10^{+0.13}_{-0.6}$
a_*	$0.9912^{+0.0015}_{-0.0025}$	$0.990^{+0.004}_{-0.002}$	$0.9851^{+0.0017}_{-0.004}$	$0.978^{+0.007}_{-0.002}$
i [deg]	$75.9^{+0.7}_{-1.3}$	$75.1^{+1.3}_{-1.3}$	$68.98^{+0.27}_{-6}$	$68.4^{+0.6}_{-0.4}$
A_{Fe}	$1.40^{+0.19}_{-0.3}$	$0.867^{+0.1}_{-0.016}$	$7.5^{+0.3}_{-1.0}$	$6.60^{+0.26}_{-1.8}$
α_{ξ}	$0.179^{+0.04}_{-0.026}$	$0.204^{+0.04}_{-0.012}$	$1.11^{+0.5}_{-0.21}$	$1.03^{+0.24}_{-0.3}$
$\log \xi$ [erg cm s $^{-1}$]	$3.15^{+0.09}_{-0.04}$	$3.27^{+0.11}_{-0.22}$	$4.70^{+P}_{-0.03}$	$4.70^{+P}_{-0.11}$
Norm	$0.00461^{+0.00011}_{-0.0002}$	$0.0073^{+0.0007}_{-0.0008}$	$0.0071^{+0.0009}_{-0.0011}$	$0.00117^{+3.8e-05}_{-2.8e-05}$
dGamma _{NICER}	$-0.172^{+0.013}_{-0.016}$	$-0.175^{+0.013}_{-0.019}$	$-0.169^{+0.018}_{-0.015}$	$-0.137^{+0.02}_{-0.017}$
crabberNorm _{NICER}	$0.745^{+0.019}_{-0.015}$	$0.741^{+0.016}_{-0.04}$	$0.738^{+0.05}_{-0.016}$	$0.792^{+0.016}_{-0.027}$
crabberNorm _{FPMB}	$1.0142^{+0.0015}_{-0.0015}$	$1.0142^{+0.0015}_{-0.0015}$	$1.0142^{+0.0015}_{-0.0015}$	$1.0142^{+0.0015}_{-0.0008}$
χ^2 /dof	804.3/706	805.4/705	812.8/706	816.4/705
	=1.13924	=1.14241	=1.15127	=1.15801
AICc	845.49	846.59	853.99	857.59
disk/total	0.53	0.46	0.036	0.044
total flux [10^{-8} ergs/cm 2 /s]	5.56	4.58	1.99	2.01
Eddington ratio (total) [$\frac{D^2}{M}$]	0.053	0.044	0.019	0.019

FIG. 6. Model and residual plots for EXO 1846–031 with *NuSTAR*+*NICER* data. In the left panel, the red lines represent the thermal components, the blue lines represent the power-law components, and orange lines represent the reflection components. In the right panel, the blue lines represent the Comptonized thermal spectra and the orange lines represent the Comptonized reflection spectra. For the lines with same color, solid lines represent the complete spectra, dotted lines represent the components scattered by the corona, and dashed lines represent the components transmitted by the corona.

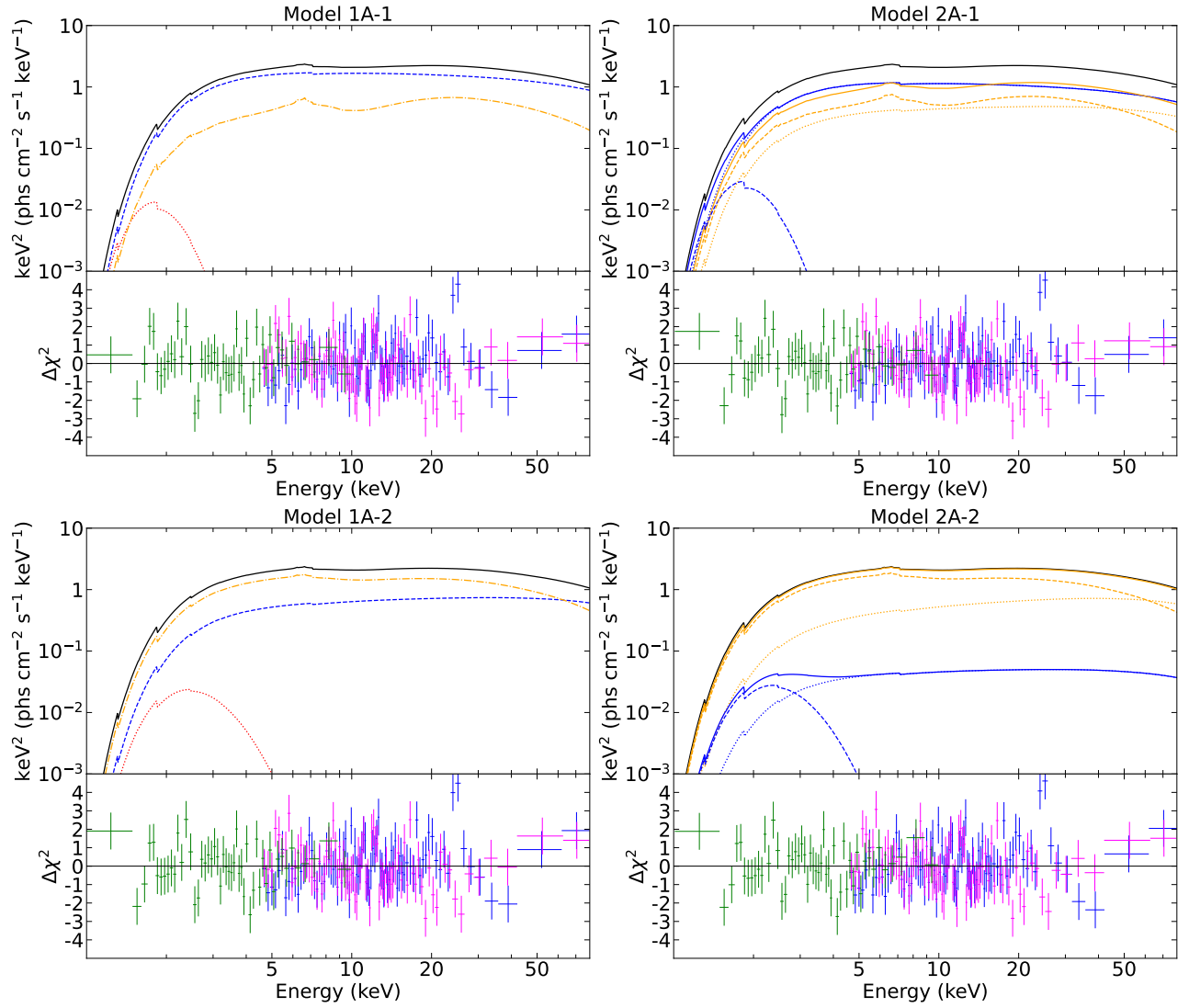
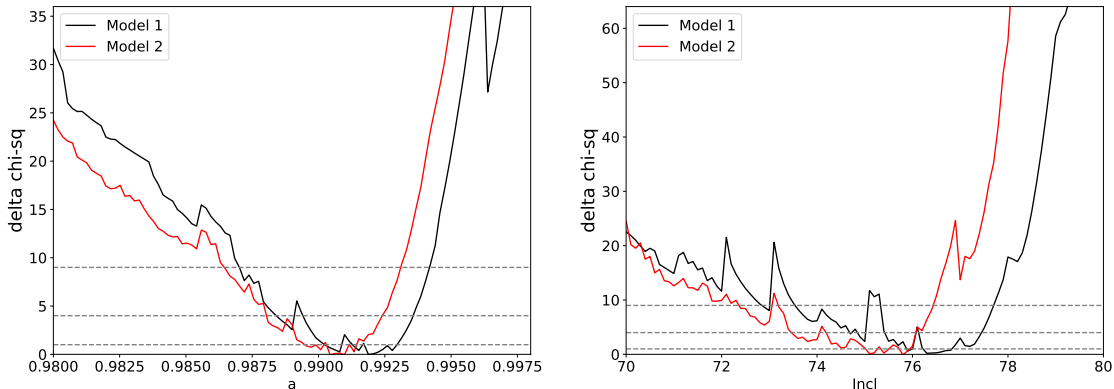


FIG. 7. The 1-D χ^2 contours for black hole spin and inclination angle for Model 1A and Model 2A with *NuSTAR* data. The horizontal dash line represents the 1σ , 2σ , 3σ confidence levels for a single parameter.



Models 1A-2 and 2A-2 are more reasonable.

From the norm of `diskbb`, we can derive an approximate inner radius [36]:

$$\text{Norm} = (r_{\text{in}}/D_{10})^2 \cos \theta, \quad (5)$$

where D_{10} is the distance in the units of 10 kpc and r_{in} is the derived inner radius from the observed data. After factoring in some correction factors [51]

$$R_{\text{in}} = \sqrt{\frac{3}{7}} \cdot \left(\frac{6}{7}\right)^3 \cdot \kappa^2 \cdot r_{\text{in}}, \quad (6)$$

where $\kappa \sim 1.7$ is the ratio of color temperature to effective temperature [52], then we can obtain R_{in} which is the true inner radius. For a Kerr black hole, R_{ISCO} (radius of the innermost stable circular orbit) can be derived from the spin [53]. Since we apply X-ray reflection spectroscopy to measure the spin, we should identify the R_{in} with R_{ISCO} [1]. Although the estimates of R_{in} and R_{ISCO} from observed data have significant uncertainty due to the lack of accurate measurements of mass and distance, R_{in} should not be much larger than R_{ISCO} given the reflection-fitting results. R_{in} inferred from the results of Model 1A-1 and 2A-1 is about $9.7\text{--}70 R_{\text{ISCO}}$ (with the same uncertainty of mass and distance in estimation of Eddington ratio), while from the results of Model 1A-2 and 2A-2 is about $1.0\text{--}2.7 R_{\text{ISCO}}$. Therefore, the best fits of Model 1A-2 and 2A-2 are somewhat favored.

C. Impact of emissivity profile

In the models with free q_{out} , we get a flat emissivity profile at large radii with $q_{\text{out}} \approx 0$. To validate these results, models with fixed q_{out} set to 3 were also examined, but they yielded significantly poorer best-fit

results ($\Delta\text{AICc} \sim 60$, as shown in Table III and Table IV) compared to the best-fit with free q_{out} in both *NuSTAR* data and *NuSTAR+NICER* data, with several parameters displaying notable differences. Additionally, models incorporating an additional `xillverCp` component were tested to explore the possibility of obtaining a larger value for q_{out} . However, the norm of `xillverCp` is consistent with zero. Furthermore, in the results of the *NuSTAR+NICER* data in Model 1A-2 and Model 2A-2, the index $q_{\text{out}} \gtrsim 1$, which alleviates concerns about a runaway emissivity for $q_{\text{out}} \sim 0$ (as illustrated in Fig. 4), so we only show the results of emissivity profile ‘‘A’’ in Table IV. Other studies also reported instances of $q_{\text{out}} \approx 0$ in GS 1354–645 [54] and GRS 1915+105 [55].

V. CONCLUSIONS

We investigated the impact of the Comptonization of the reflection spectrum in the case of EXO 1846–031. We have drawn the following conclusions:

1. Considering reflection Comptonization by using `simplcutx` does not yield a significantly different best fit and it does not affect the values of key parameters such as black hole spin and inclination angle. In the case of coronal properties evolving during state transitions, the variation in f_{SC} potentially providing a useful consistency check.

2. The inclusion of soft X-ray data does not significantly affect the estimations of key parameters, but gives a new fit with more reasonable luminosity, inner radius of disk and emissivity profile. The fit of *NuSTAR+NICER* data with a weak disk component and non-zero q_{out} is the most reasonable in this case.

Acknowledgments – This work was supported by

the Natural Science Foundation of Shanghai, Grant No. 22ZR1403400, and the National Natural Science

Foundation of China (NSFC), Grant No. 12250610185, 11973019, and 12261131497.

-
- [1] C. Bambi, L. W. Brenneman, T. Dauser, J. A. García, V. Grinberg, A. Ingram, J. Jiang, H. Liu, A. M. Lohfink, A. Marinucci, G. Mastroserio, R. Middei, S. Nampalliwar, A. Niedźwiecki, J. F. Steiner, A. Tripathi, and A. A. Zdziarski, *Space Sci. Rev.* **217**, 65 (2021).
- [2] A. C. Fabian, K. Nandra, C. S. Reynolds, W. N. Brandt, C. Otani, Y. Tanaka, H. Inoue, and K. Iwasawa, *Mon. Not. R. Astron. Soc.* **277**, L11 (1995), [arXiv:astro-ph/9507061 \[astro-ph\]](#).
- [3] A. Zoghbi, A. C. Fabian, P. Uttley, G. Miniutti, L. C. Gallo, C. S. Reynolds, J. M. Miller, and G. Ponti, *Mon. Not. R. Astron. Soc.* **401**, 2419 (2010), [arXiv:0910.0367 \[astro-ph.HE\]](#).
- [4] G. Risaliti, F. A. Harrison, K. K. Madsen, D. J. Walton, S. E. Boggs, F. E. Christensen, W. W. Craig, B. W. Grefenstette, C. J. Hailey, E. Nardini, D. Stern, and W. W. Zhang, *Nature (London)* **494**, 449 (2013), [arXiv:1302.7002 \[astro-ph.HE\]](#).
- [5] I. D. Novikov and K. S. Thorne, in *Black Holes (Les Astres Occlus)* (1973) pp. 343–450.
- [6] R. R. Ross and A. C. Fabian, *Mon. Not. R. Astron. Soc.* **358**, 211 (2005), [arXiv:astro-ph/0501116 \[astro-ph\]](#).
- [7] J. García and T. R. Kallman, *Astrophys. J.* **718**, 695 (2010), [arXiv:1006.0485 \[astro-ph.HE\]](#).
- [8] J. F. Steiner, R. A. Remillard, J. A. García, and J. E. McClintock, *Astrophys. J.* **829**, L22 (2016), [arXiv:1609.04592 \[astro-ph.HE\]](#).
- [9] J. F. Steiner, J. A. García, W. Eikmann, J. E. McClintock, L. W. Brenneman, T. Dauser, and A. C. Fabian, *Astrophys. J.* **836**, 119 (2017), [arXiv:1701.03777 \[astro-ph.HE\]](#).
- [10] D. R. Wilkins and L. C. Gallo, *Mon. Not. R. Astron. Soc.* **448**, 703 (2015), [arXiv:1412.0015 \[astro-ph.HE\]](#).
- [11] A. N. Parmar and N. E. White, *IAU Circ.* **4051**, 1 (1985).
- [12] H. Negoro, M. Nakajima, S. Sugita, R. Sasaki, W. I. T. Mihara, W. Maruyama, M. Aoki, K. Kobayashi, T. Tamagawa, M. Matsuoka, T. Sakamoto, M. Serino, H. Nishida, A. Yoshida, Y. Tsuboi, H. Kawai, T. Sato, M. Shidatsu, N. Kawai, M. Sugizaki, M. Oeda, K. Shiraishi, S. Nakahira, Y. Sugawara, S. Ueno, H. Tomida, M. Ishikawa, N. Isobe, R. Shimomukai, M. Tomimaga, Y. Ueda, A. Tanimoto, S. Yamada, S. Ogawa, K. Setoguchi, T. Yoshitake, H. Tsunemi, T. Yoneyama, K. Asakura, S. Ide, M. Yamauchi, S. Iwahori, Y. Kurihara, K. Kurogi, K. Miike, T. Kawamuro, K. Yamaoka, and Y. Kawakubo, *The Astronomer’s Telegram* **12968**, 1 (2019).
- [13] I. A. Mereminskiy, R. A. Krivonos, P. S. Medvedev, and S. A. Grebenev, *The Astronomer’s Telegram* **12969**, 1 (2019).
- [14] P. M. Bult, K. C. Gendreau, Z. Arzoumanian, T. E. Strohmayer, P. S. Ray, S. Guillot, W. Iwakiri, J. Homan, D. Altamirano, G. K. Jaisawal, and J. M. Miller, *The Astronomer’s Telegram* **12976**, 1 (2019).
- [15] J. M. Miller, A. Zoghbi, P. Gandhi, and J. Paice, *The Astronomer’s Telegram* **13012**, 1 (2019).
- [16] Y.-J. Yang, R. Soria, D. Russell, G. Xiao, J. Qu, and S.-N. Zhang, *The Astronomer’s Telegram* **13036**, 1 (2019).
- [17] Y.-J. Yang, G. Xiao, R. Soria, D. Russell, J. Qu, and S.-N. Zhang, *The Astronomer’s Telegram* **13037**, 1 (2019).
- [18] P. A. Draghis, J. M. Miller, E. M. Cackett, E. S. Kammoun, M. T. Reynolds, J. A. Tomsick, and A. Zoghbi, *Astrophys. J.* **900**, 78 (2020), [arXiv:2007.04324 \[astro-ph.HE\]](#).
- [19] A. B. Abdikamalov, D. Ayzenberg, C. Bambi, H. Liu, and Y. Zhang, *Phys. Rev. D* **103**, 103023 (2021), [arXiv:2101.10100 \[astro-ph.HE\]](#).
- [20] A. Tripathi, A. B. Abdikamalov, D. Ayzenberg, C. Bambi, and H. Liu, *Astrophys. J.* **913**, 129 (2021), [arXiv:2102.04695 \[astro-ph.HE\]](#).
- [21] A. Tripathi, B. Zhou, A. B. Abdikamalov, D. Ayzenberg, and C. Bambi, *JCAP* **2021**, 002 (2021), [arXiv:2103.07593 \[astro-ph.HE\]](#).
- [22] Z. Yu, Q. Jiang, A. B. Abdikamalov, D. Ayzenberg, C. Bambi, H. Liu, S. Nampalliwar, and A. Tripathi, *Phys. Rev. D* **104**, 084035 (2021), [arXiv:2106.11658 \[astro-ph.HE\]](#).
- [23] J. Gu, S. Riaz, A. B. Abdikamalov, D. Ayzenberg, and C. Bambi, *European Physical Journal C* **82**, 708 (2022), [arXiv:2206.14733 \[gr-qc\]](#).
- [24] J. Tao, S. Riaz, B. Zhou, A. B. Abdikamalov, C. Bambi, and D. Malafarina, *Phys. Rev. D* **108**, 083036 (2023), [arXiv:2301.12164 \[gr-qc\]](#).
- [25] H.-X. Liu, Y. Huang, G.-C. Xiao, Q.-C. Bu, J.-L. Qu, S. Zhang, S.-N. Zhang, S.-M. Jia, F.-J. Lu, X. Ma, L. Tao, W. Zhang, L. Chen, L.-M. Song, T.-P. Li, Y.-P. Xu, X.-L. Cao, Y. Chen, C.-Z. Liu, C. Cai, Z. Chang, G. Chen, T.-X. Chen, Y.-B. Chen, Y.-P. Chen, W. Cui, W.-W. Cui, J.-K. Deng, Y.-W. Dong, Y.-Y. Du, M.-X. Fu, G.-H. Gao, H. Gao, M. Gao, M.-Y. Ge, Y.-D. Gu, J. Guan, C.-C. Guo, D.-W. Han, J. Huo, L.-H. Jiang, W.-C. Jiang, J. Jin, Y.-J. Jin, L.-D. Kong, B. Li, C.-K. Li, G. Li, M.-S. Li, W. Li, X. Li, X.-B. Li, X.-F. Li, Y.-G. Li, Z.-W. Li, X.-H. Liang, J.-Y. Liao, B.-S. Liu, G.-Q. Liu, H.-W. Liu, X.-J. Liu, Y.-N. Liu, B. Lu, X.-F. Lu, Q. Luo, T. Luo, B. Meng, Y. Nang, J.-Y. Nie, G. Ou, N. Sai, R.-C. Shang, X.-Y. Song, L. Sun, Y. Tan, Y.-L. Tuo, C. Wang, G.-F. Wang, J. Wang, L.-J. Wang, W.-S. Wang, Y.-S. Wang, X.-Y. Wen, B.-Y. Wu, B.-B. Wu, M. Wu, S. Xiao, S.-L. Xiong, H. Xu, J.-W. Yang, S. Yang, Y.-J. Yang, Y.-J. Yang, Q.-B. Yi, Q.-Q. Yin, Y. You, A.-M. Zhang, C.-M. Zhang, F. Zhang, H.-M. Zhang, J. Zhang, T. Zhang, W.-C. Zhang, W.-Z. Zhang, Y. Zhang, Y.-F. Zhang, Y.-J. Zhang, Y.-H. Zhang, Y. Zhang, Z. Zhang, Z. Zhang, Z.-L. Zhang, H.-S. Zhao, X.-F. Zhao, S.-J. Zheng, Y.-G. Zheng, D.-K. Zhou, J.-F. Zhou, Y.-X. Zhu, R.-L. Zhuang, and Y. Zhu, *Research in Astronomy and Astrophysics* **21**, 070 (2021), [arXiv:2009.10956 \[astro-ph.HE\]](#).
- [26] Y. Wang, L. Ji, J. A. García, T. Dauser, M. Méndez, J. Mao, L. Tao, D. Altamirano, P. Maggi, S. N. Zhang, M. Y. Ge, L. Zhang, J. L. Qu, S. Zhang, X. Ma, F. J. Lu, T. P. Li, Y. Huang, S. J. Zheng, Z. Chang, Y. L. Tuo, L. M. Song, Y. P. Xu, Y. Chen, C. Z. Liu, Q. C. Bu, C. Cai, X. L. Cao, L. Chen, T. X. Chen, Y. P. Chen,

- W. W. Cui, Y. Y. Du, G. H. Gao, Y. D. Gu, J. Guan, C. C. Guo, D. W. Han, J. Huo, S. M. Jia, W. C. Jiang, J. Jin, L. D. Kong, B. Li, C. K. Li, G. Li, W. Li, X. Li, X. B. Li, X. F. Li, Z. W. Li, X. H. Liang, J. Y. Liao, H. W. Liu, X. J. Liu, X. F. Lu, Q. Luo, T. Luo, B. Meng, Y. Nang, J. Y. Nie, G. Ou, N. Sai, R. C. Shang, X. Y. Song, L. Sun, Y. Tan, W. S. Wang, Y. D. Wang, Y. S. Wang, X. Y. Wen, B. B. Wu, B. Y. Wu, M. Wu, G. C. Xiao, S. Xiao, S. L. Xiong, S. Yang, Y. J. Yang, Q. B. Yi, Q. Q. Yin, Y. You, F. Zhang, H. M. Zhang, J. Zhang, W. C. Zhang, W. Zhang, Y. F. Zhang, H. S. Zhao, X. F. Zhao, and D. K. Zhou, *Astrophys. J.* **906**, 11 (2021), [arXiv:2010.14662 \[astro-ph.HE\]](#).
- [27] X. Q. Ren, Y. Wang, S. N. Zhang, R. Soria, L. Tao, L. Ji, Y. J. Yang, J. L. Qu, S. Zhang, L. M. Song, M. Y. Ge, Y. Huang, X. B. Li, J. Y. Liao, H. X. Liu, R. C. Ma, Y. L. Tuo, P. J. Wang, W. Zhang, and D. K. Zhou, *Astrophys. J.* **932**, 66 (2022), [arXiv:2205.04635 \[astro-ph.HE\]](#).
- [28] K. K. Madsen, K. Forster, B. Grefenstette, F. A. Harrison, and H. Miyasaka, *Journal of Astronomical Telescopes, Instruments, and Systems* **8**, 034003 (2022), [arXiv:2110.11522 \[astro-ph.IM\]](#).
- [29] J. S. Kaastra and J. A. M. Bleeker, *Astron. Astrophys.* **587**, A151 (2016), [arXiv:1601.05309 \[astro-ph.IM\]](#).
- [30] R. A. Remillard, M. Loewenstein, J. F. Steiner, G. Y. Prigozhin, B. LaMarr, T. Enoto, K. C. Gendreau, Z. Arzoumanian, C. Markwardt, A. Basak, A. L. Stevens, P. S. Ray, D. Altamirano, and D. J. K. Buisson, *Astron. J.* **163**, 130 (2022), [arXiv:2105.09901 \[astro-ph.IM\]](#).
- [31] K. A. Arnaud, in *Astronomical Data Analysis Software and Systems V*, Astronomical Society of the Pacific Conference Series, Vol. 101, edited by G. H. Jacoby and J. Barnes (1996) p. 17.
- [32] L. Tao, J. A. Tomsick, J. Qu, S. Zhang, S. Zhang, and Q. Bu, *Astrophys. J.* **887**, 184 (2019), [arXiv:1910.11979 \[astro-ph.HE\]](#).
- [33] S. K. Nath, D. Debnath, K. Chatterjee, R. Bhowmick, H.-K. Chang, and S. K. Chakrabarti, *Astrophys. J.* **960**, 5 (2024), [arXiv:2307.04522 \[astro-ph.HE\]](#).
- [34] J. Wilms, A. Allen, and R. McCray, *Astrophys. J.* **542**, 914 (2000), [arXiv:astro-ph/0008425 \[astro-ph\]](#).
- [35] J. E. Pringle, *Annu. Rev. Astron. Astrophys.* **19**, 137 (1981).
- [36] K. Mitsuda, H. Inoue, K. Koyama, K. Makishima, M. Matsuoka, Y. Ogawara, N. Shibasaki, K. Suzuki, Y. Tanaka, and T. Hirano, *Publ. Astron. Soc. Japan* **36**, 741 (1984).
- [37] A. A. Zdziarski, W. N. Johnson, and P. Magdziarz, *Monthly Notices of the Royal Astronomical Society* **283**, 193 (1996).
- [38] P. T. Życki, C. Done, and D. A. Smith, *Mon. Not. R. Astron. Soc.* **309**, 561 (1999), [arXiv:astro-ph/9904304 \[astro-ph\]](#).
- [39] R. K. Smith, L. A. Valencic, and L. Corrales, *Astrophys. J.* **818**, 143 (2016), [arXiv:1602.07766 \[astro-ph.HE\]](#).
- [40] E. Barillier, V. Grinberg, D. Horn, M. A. Nowak, R. A. Remillard, J. F. Steiner, D. J. Walton, and J. Wilms, *Astrophys. J.* **944**, 165 (2023), [arXiv:2301.09226 \[astro-ph.HE\]](#).
- [41] J. F. Steiner, J. E. McClintock, R. A. Remillard, L. Gou, S. Yamada, and R. Narayan, *Astrophys. J.* **718**, L117 (2010), [arXiv:1006.5729 \[astro-ph.HE\]](#).
- [42] K. P. Burnham, A practical information-theoretic approach (1998).
- [43] H. Akaike, *IEEE Transactions on Automatic Control* **19**, 716 (1974).
- [44] Y. Dong, Z. Liu, Y. Tuo, J. F. Steiner, M. Ge, J. A. García, and X. Cao, *Mon. Not. R. Astron. Soc.* **514**, 1422 (2022), [arXiv:2205.12058 \[astro-ph.HE\]](#).
- [45] H. Liu, C. Bambi, J. Jiang, J. A. García, L. Ji, L. Kong, X. Ren, S. Zhang, and S. Zhang, *Astrophys. J.* **950**, 5 (2023), [arXiv:2211.09543 \[astro-ph.HE\]](#).
- [46] Q. Liu, H. Liu, C. Bambi, and L. Ji, *Mon. Not. R. Astron. Soc.* **512**, 2082 (2022), [arXiv:2111.00719 \[astro-ph.HE\]](#).
- [47] J. Wang, E. Kara, M. Lucchini, A. Ingram, M. van der Klis, G. Mastroserio, J. A. García, T. Dauser, R. Connors, A. C. Fabian, J. F. Steiner, R. A. Remillard, E. M. Cackett, P. Uttley, and D. Altamirano, *Astrophys. J.* **930**, 18 (2022), [arXiv:2205.00928 \[astro-ph.HE\]](#).
- [48] T. E. Strohmayer and Nicer Observatory Science Working Group, in *American Astronomical Society Meeting Abstracts #235*, American Astronomical Society Meeting Abstracts, Vol. 235 (2020) p. 159.02.
- [49] A. N. Parmar, L. Angelini, P. Roche, and N. E. White, *Astron. Astrophys.* **279**, 179 (1993).
- [50] D. R. A. Williams, S. E. Motta, R. Fender, J. C. A. Miller-Jones, J. Neilsen, J. R. Allison, J. Bright, I. Heywood, P. F. L. Jacob, L. Rhodes, E. Tremou, P. A. Woudt, J. v. d. Eijnden, F. Carotenuto, D. A. Green, D. Titterton, A. J. van der Horst, and P. Saikia, *Mon. Not. R. Astron. Soc.* **517**, 2801 (2022), [arXiv:2209.10228 \[astro-ph.HE\]](#).
- [51] A. Kubota, Y. Tanaka, K. Makishima, Y. Ueda, T. Dotani, H. Inoue, and K. Yamaoka, *Publ. Astron. Soc. Japan* **50**, 667 (1998).
- [52] T. Shimura and F. Takahara, *Astrophys. J.* **445**, 780 (1995).
- [53] J. M. Bardeen, W. H. Press, and S. A. Teukolsky, *Astrophys. J.* **178**, 347 (1972).
- [54] Y. Xu, S. Nampalliwar, A. B. Abdikamalov, D. Ayzenberg, C. Bambi, T. Dauser, J. A. García, and J. Jiang, *Astrophys. J.* **865**, 134 (2018), [arXiv:1807.10243 \[gr-qc\]](#).
- [55] Y. Zhang, A. B. Abdikamalov, D. Ayzenberg, C. Bambi, and S. Nampalliwar, *Astrophys. J.* **884**, 147 (2019), [arXiv:1907.03084 \[gr-qc\]](#).